Chapter

Surface Plasmons in Oxide Semiconductor Nanoparticles: Effect of Size and Carrier Density

Hiroaki Matsui

Abstract

Oxide semiconductors have received much attention for potential use in optoelectronic applications such as transparent electrodes, transistors, and emitting devices. Recently, new functionalities of oxide semiconductors have been discovered such as localized surface plasmon resonances (LSPRs), which show high-efficiency plasmon excitations in the infrared (IR) range using different structures such as nanorods, nanoparticles (NPs), and nanodots. In this chapter, we introduce optical properties of carrier- and size-dependent LSPRs in oxide semiconductor NPs based on In_2O_3: Sn (ITO). In particular, systematic examinations of carrier- and size-dependent LSPRs reveal the damping mechanisms on LSPR excitations of ITO NPs, which play an important role in determining excitation efficiency of LSPRs. Additionally, the control of carrier and size in the ITO NPs contribute toward improving solar-thermal shielding in the IR range. The high IR reflectance of assembled films of ITO NPs is due to three-dimensional plasmon coupling between the NPs, which is related to electron carriers and particle size of ITO NPs. This chapter provides new information concerning structural design when fabricating thermal-shielding materials based on LSPRs in oxide semiconductor NPs.

Keywords: oxide semiconductor, nanocrystal, plasmon, infrared, energy-saving

1. Introduction

Metals (such as Au and Ag) have been utilized for the majority of plasmonic materials in the visible range. Recently, oxide semiconductors have attracted much attention for use as potential new plasmonic materials. In particular, ZnO: Ga and In_2O_3: Sn (ITO) are known for use as transparent electrodes due to their metallic conductivity. These oxide semiconductors show surface plasmon resonances (SPRs) in the infrared (IR) range [1, 2]. Propagated SPRs can be excited on metal surfaces using a prism-coupling technique such as a Kretschmann-type attenuated total reflection (ATR) system [3]. Our research group has investigated the optical properties of SPRs excited on ZnO: Ga and ITO film surfaces from the viewpoint of physical characteristics such as field strength and penetration depth [4–6]. On the other hand, subwavelength materials such as nanorods, nanoparticles (NPs), and nanodots are capable of supporting localized surface plasmon resonances (LSPRs), which can be directly excited by incident light in the absence of a prism-coupling method [7, 8]. Above all, LSPRs confined to NPs can lead to light at the nanoscale

when confining the collective oscillations of free electrons into NPs. This LSPR effect further provides strong electric fields (*E*-fields) on NP surfaces, which contribute to surface-enhanced optical spectroscopy [9]. For example, assembled films consisting of ITO NPs have demonstrated optical enhancements of near-IR luminescence and absorption in the IR range [10, 11]. Therefore, optical studies concerning oxide semiconductor NPs can break new research ground in the area of plasmonics and metamaterials.

An understanding of plasmon damping is very important in order to achieve high-efficiency LSPRs. A number of plasmonic studies of metal NPs have been devoted to investigating the damping processes of LSPRs. For metal NPs, there are two main damping processes, comprising (i) size-dependent surface scattering and (ii) electronic structure-related inter- and intraband damping [12–15]. The damping processes are closely related to the physical properties of the metals. Therefore, understanding of the damping processes of LSPRs in oxide semiconductor NPs is also important for the control of optical properties. Oxide semiconductor NPs are useful plasmonic materials since their LSPR wavelengths can be widely tuned by electron density in addition to particle size [16–18]. Carrier control of LSPRs indicates that oxide semiconductors have an additional means of tuning the optical properties in a manner that is not as readily available for metal NPs. In particular, carrier-dependent damping is a specific feature of the plasmonic response in oxide semiconductor NPs. Precise elucidation of the carrier-dependent damping process including structural size is required for the optical design of plasmonic materials based on oxide semiconductor NPs.

The purpose of this chapter is to report on the light interactions of size- and carrier-controlled ITO NPs and to discuss their plasmonic applications in the IR range. We introduce size- and carrier-dependent plasmonic responses and provide information for the physical interpretation of optical spectra. A rigorous approach to the analysis of the optical properties allows us to show a quantitative assessment of the electronic properties in ITO NPs. The employments of Mie theoretical calculations, which can describe well the optical properties of metal NPs, are validated in terms of ITO NPs. Finally, we discuss the optical properties assembled films of ITO NPs for solar-thermal shielding.

2. Carriers and plasmon excitations

2.1 Synthesis of ITO NPs

ITO NPs with different Sn contents were fabricated using the chemical thermolysis method with various initial ratios of precursor complexes $(C_{10}H_{22}O_2)_3In$ and $(C_{10}H_{22}O_2)_4Sn$ [19]. Indium and tin complexes were thermal heated at 300–350°C for 4 h in a reducing agent, and the mixture was then gradually cooled to room temperature. The resultant mixture produced a pale blue suspension and to which was then added excess ethanol to induce precipitation. Centrifugation and repeated washing were conducted four times using ethanol, which produced dried powders of ITO NPs with a pale blue color. Finally, the powder samples were dispersed in a nonpolar solvent of toluene. Electrophoresis analysis revealed a positive zeta potential of +31 meV for the NPs, which indicated the NPs had non-aggregated states in the solvent due to electrostatic repulsion between NPs. Particle surfaces of the NPs were terminated by organic ligands consisting of fatty acids, which contributed in spatial separation between NPs.

2.2 Carrier-dependent plasmon absorptions

Optical absorptions and TEM images of ITO NPs with different electron densities (n_e) were examined (**Figure 1**). TEM images revealed that all NP sizes (D) were ca. 36 nm (**Figure 2(a–c)**). This indicates that the systematic change in the absorption spectra is related to the Sn content. Absorption measurements were performed using a Fourier-transform infrared (FT-IR) spectrometer. A value of n_e was estimated from the absorption spectra by theoretical calculations. The following equation was used to derive absorption intensity (A) from the experimental data [20]:

$$A = 4\pi kR^3 \mathrm{Im}\left\{\frac{\varepsilon_m(\omega) - \varepsilon_d}{\varepsilon_m(\omega) + 2\varepsilon_d}\right\} \quad (1)$$

where $k = 2\pi(\varepsilon_d)^{1/2}\omega/c$ with c representing the speed of light, ε_d indicates the host dielectric constants of toluene, $\varepsilon_m(\omega)$ is the particle dielectric function, and R is

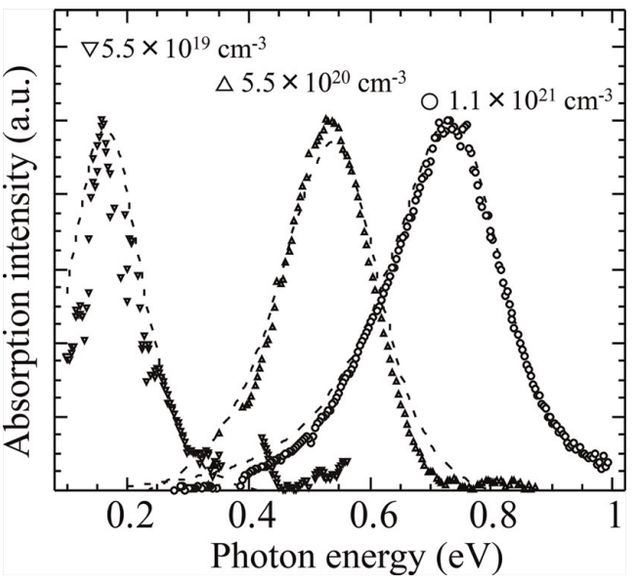

Figure 1.
Absorption spectra of ITO NPs with different electron densities. Doping with Sn contents of 0.02, 1, and 5% into the NPs' induced electron density of 6.3 × 10¹⁹ cm⁻³, 5.7 × 10²⁰ cm⁻³, and 1.1 × 10²¹ cm⁻³, respectively. Dot lines indicate theoretical calculations based on the modified Mie theory [19].

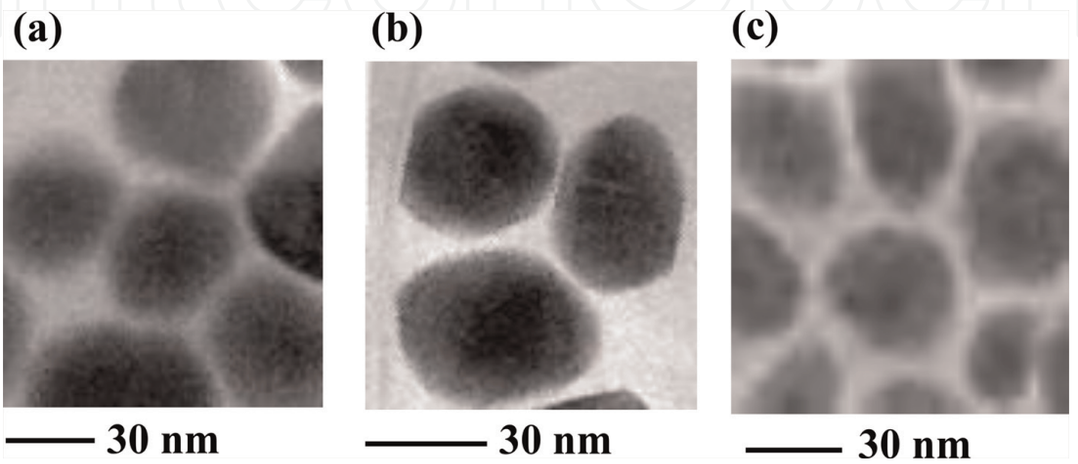

Figure 2.
TEM images of ITO NPs with electron densities of (a) 6.3 × 10¹⁹ cm⁻³, (b) 5.7 × 10²⁰ cm⁻³, and (c) 1.1 × 10²¹ cm⁻³ [19].

the particle radius. Furthermore, $\varepsilon_m(\omega)$ employed the free-electron Drude term with frequency-dependent damping constant, $\Gamma(\omega)$, on the basis that ITO comprised free-electron carriers [20]:

$$\varepsilon_m(\omega) = 1 - \frac{\omega_p^2}{\omega(\omega + i\Gamma)} \tag{2}$$

The plasma frequency (ω_p) is given by $\omega_p^2 = ne/\varepsilon_\infty \varepsilon_0 m^*$, where ε_∞ is the high-frequency dielectric constant, ε_0 is the vacuum permittivity, and m^* is the effective electron mass. Fitted absorptions were used with parameter values of ε_d = 2.03 (n = 1.426 refractive index of the solvent), ε_∞ = 3.8, and m^* = 0.3 m_0 to estimate $\varepsilon_p(\omega)$.The term $\Gamma(\omega)$ based on electron-impurity scattering can be described by the following relation [21]:

$$\Gamma(\omega) = f(\omega)\Gamma_L + [1 - f(\omega)]\Gamma_H \left(\frac{\omega}{\Gamma_H}\right)^{-3/2} \tag{3}$$

where $f(\omega)$ can be described by $f(\omega) = [1 + \exp\{(\omega - \Gamma_x)/\sigma\}]^{-1}$. Γ_H and Γ_L represent the high-frequency ($\omega = \infty$) and low-frequency ($\omega = 0$) damping, respectively. Γ_X and σ represent the change-over frequency and width of the function, respectively.

Calculated absorption spectra were very close to the experimental data. ITO NPs doped with Sn content of 0.02, 1, or 5% provided electron density of 6.3×10^{19}, 5.7×10^{20}, and 1.1×20^{21} cm^{-3}, respectively (**Figure 1**). We summarized the LSPR resonant peak and absorption intensity as a function of n_e (**Figure 3(a)**). The LSPR resonant peak gradually showed a redshift from the near-IR to mid-IR range with decreasing n_e. Additionally, the absorption intensity decreased markedly with decreasing n_e. No plasmon excitation was observed in the low n_e region below 10^{19} cm^{-3}. The Mott critical density (N_c) of ITO is estimated as $N_c = 6 \times 10^{18}$ cm^{-3} (**Figure 3(b)**). Below the Mott critical density, the impurity band is not overlapped with the Fermi energy (E_F) level. ITO results in a band insulator.

However, the E_F level combined with the impurity band in the middle n_e region from 10^{19} to 10^{20} cm^{-3}. At the high n_e region above 10^{20} cm^{-3}, the E_F level is placed in a highest occupied state in the conduction band (CB). As a consequence, ITO

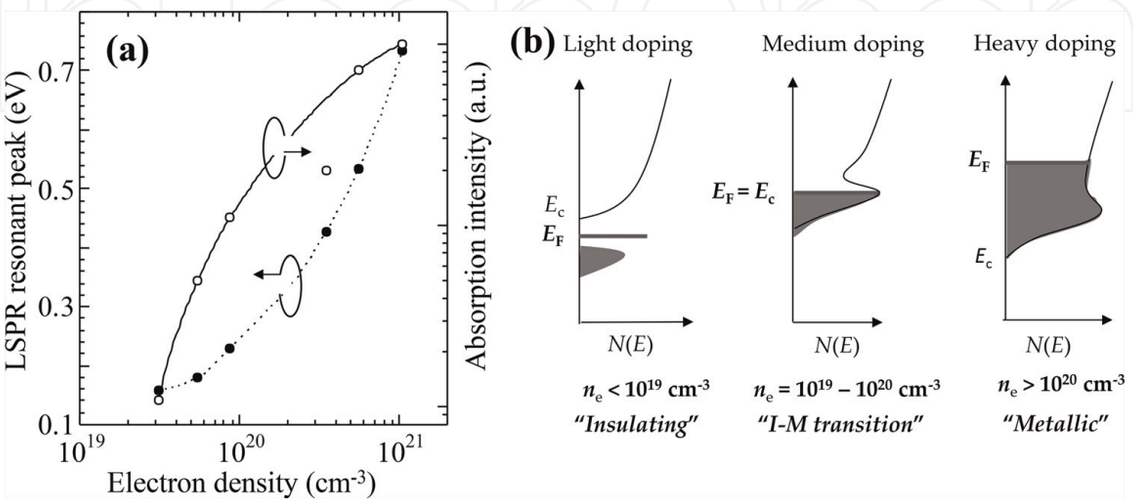

Figure 3.
(a) LSPR resonant peak and absorption intensity of ITO NPs as a function of electron density. (b) a schematic picture of electronic structures of ITO with different ranges of electron density.

shows metallic behavior. These results indicated that a large amount of free electrons were required to excite highly efficient plasmon excitations. ITO NPs were suitable for plasmonic materials in the near-IR range.

2.3 Damping mechanism

The two types of damping processes that exist in plasmon excitations of metal NPs are (i) bulk damping and (ii) surface damping. Bulk damping (γ_B) is related to electron-electron ($\gamma_{e\text{-}e}$), electron-phonon ($\gamma_{e\text{-}ph.}$), and electron-impurity scattering ($\gamma_{e\text{-impurity}}$). These scattering components determine a mean free path (l_m) of a free electron. On the other hand, surface scattering is effective when a NP size is smaller than l_m, which becomes the main damping process in NPs.

Surface scattering (γ_s) can be described by $\gamma_s = Av_F/l_{SC}$ for a small nanoparticle, where A is a material constant and v_F is the Fermi velocity [$v_F = \hbar/m^*(3\pi n_e)^{1/3}$]. The surface scattering length (l_{SC}) is defined by $l_{SC} = 4\ V/S$, where V is the volume and S is the surface area of the particle [20]. For our ITO NPs, l_{SC} was calculated as 24 nm, which was longer than the l_m of ITO (~10 nm) [22, 23]. For ITO NPs, no surface scattering was effective because the l_m of ITO was smaller than l_{SC}. Therefore, it is considered that ITO NPs are mainly related to bulk damping.

Metallic conductivity of ITO NPs is obtained by doping with impurity atoms, suggesting that ITO NPs involve electron-impurity scattering in bulk damping. The spectral features of ITO NPs could be fitted using Mie theory with frequency-dependent damping parameter $\Gamma(\omega)$. **Figure 4(a)** shows absorption spectra of ITO NPs with lowest (5.5×10^{19} cm^{-3}) and highest (1.1×10^{21} cm^{-3}) n_e values. For NPs with the lowest n_e, a symmetric absorption spectrum was obtained, while an asymmetric spectrum was obtained for NPs with the highest n_e. These spectral features were determined by Γ_H and Γ_L. **Figure 4(b)** shows the dependence of Γ_H and Γ_L on electron density. A difference in Γ_H and Γ_L values was found in the high n_e region above 10^{20} cm^{-3}. Electron-impurity scattering is reflected by Γ_L, providing asymmetric LSPR features by broadening in the low photon energy regions. In contrast, the Γ_L values (~70 meV) were the same as those of Γ_H in the low n_e region below 10^{20} cm^{-3}, indicating that LSPRs were independent of electron-impurity scattering.

The carrier-dependent plasmon response is divided into two n_e regions. Region-I comprises low n_e below 10^{20} cm^{-3}, in which coherence of electron oscillation in ITO NPs is not always disturbed by electron-impurity scattering. The spectral features of LSPRs comprise narrow line-widths and symmetric line-shapes. However, absorption intensity is small (**Figure 3(a)**) since a short mean free path length (l_m = 3–4 nm) determines the coherence of electron oscillations in the NPs. This situation is due to insufficient conduction paths. Region-II comprises high n_e above 10^{20} cm^{-3}, in which LSPR excitations become more effective with increasing l_m, as a result of increased n_e. The l_m value of NPs with the highest n_e was estimated as 10.7 nm. However, LSPR excitations are influenced by electron-impurity scattering, which generated the asymmetric line-shapes.

Degenerated metals on doped oxide semiconductors are generally realized by extrinsic and/or intrinsic dopants. However, the carrier screening effect from background cations is weak in contrast to metals with a short screening length (comprising several angstroms) [24]. Electron-impurity scattering dominates the optical properties of LSPRs in the high n_e region. In this work, the maximum lm in ITO NPs was 10.7 nm. Previous reports have detailed long l_m values from 14 to 16 nm on ITO films [22, 23]. Control of crystallinity and impurities in ITO NPs will be required to obtain high-efficiency LSPR excitations in the IR range.

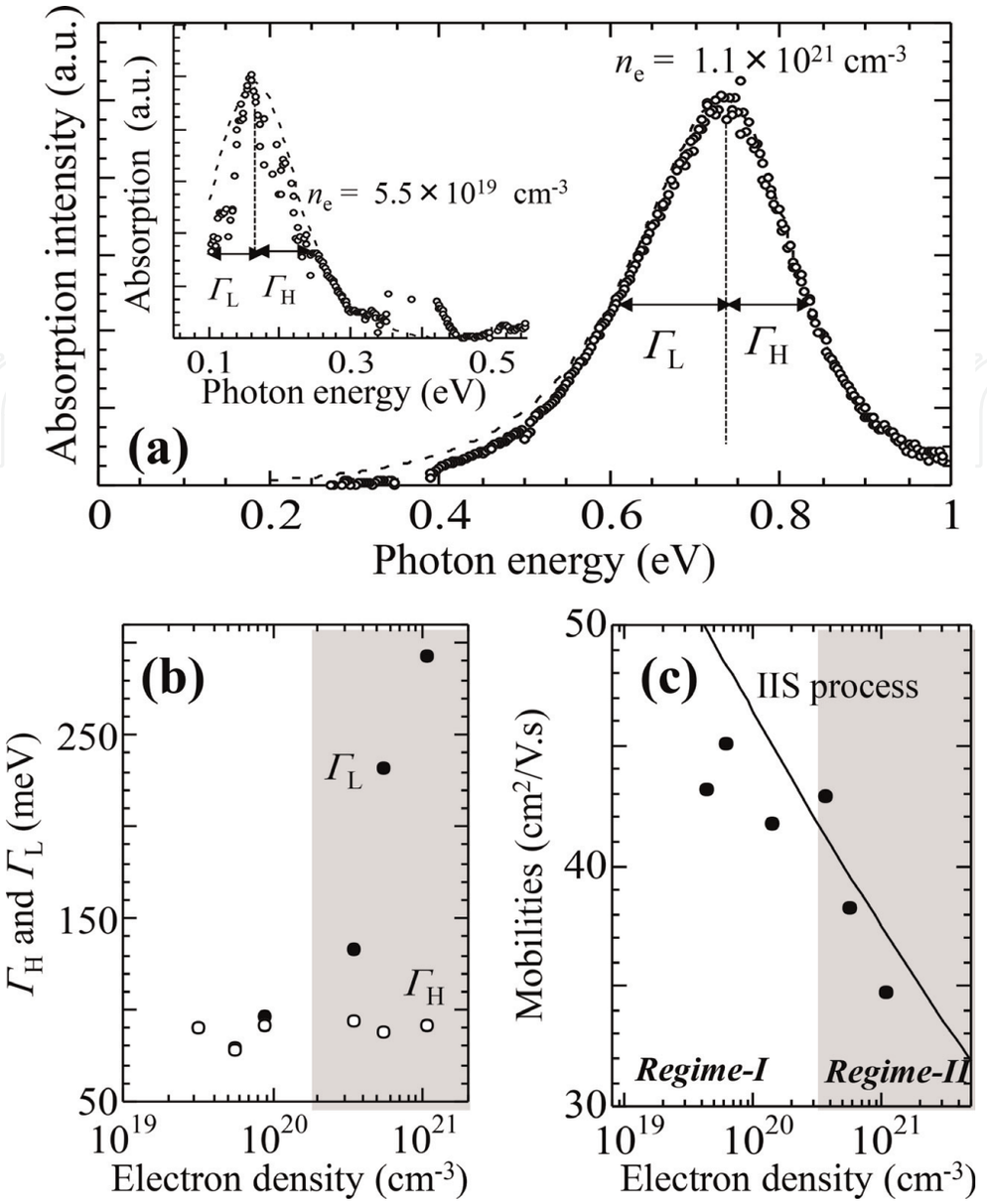

Figure 4.
(a) Absorption spectra of ITO NPs with n_e values of 5.5 × 10^{19} and 1.1 × 10^{21} cm^{-3}. (b) Dependence of Γ_H (●) and Γ_L (○) on electron density. (c) Mobility (μ_e) as a function of electron density. The μ_e (black dots) are compared with those obtained using ionized impurity scattering (IIS) process (black line).

3. Particle size and plasmon excitations

Figure 5(a) shows the size distribution of ITO NPs, revealing that size distribution gradually increased with increasing particle size (D): D = 10 ± 2.2 nm, 20 ± 3.5 nm, and 36 ± 4.3 nm. **Figure 6** shows TEM results of the dependency of NPs on particle size. In particular, NPs with D = 36 nm showed well-developed facet surfaces, and NPs were clearly separated from one another due to the presence of organic ligands formed on the NP surfaces. All NP samples showed broad peak characteristic of colloid NPs with a crystalline nature (**Figure 5(b)**). Patterns were similar to those of standard cubic bixbyite, which had no discernible SnO or SnO_2 peak. Besides, the line-width of the (222) peak, $\Delta(2\theta)$, was narrower for the NPs with D = 36 nm than D = 10 nm. These results reflected differences in crystallinity, size, defects, and strain in the NPs.

The absorption spectra of the NPs with different particle sizes are shown in **Figure 7(a)**. Based on the Mie theory with frequency-dependent damping, the

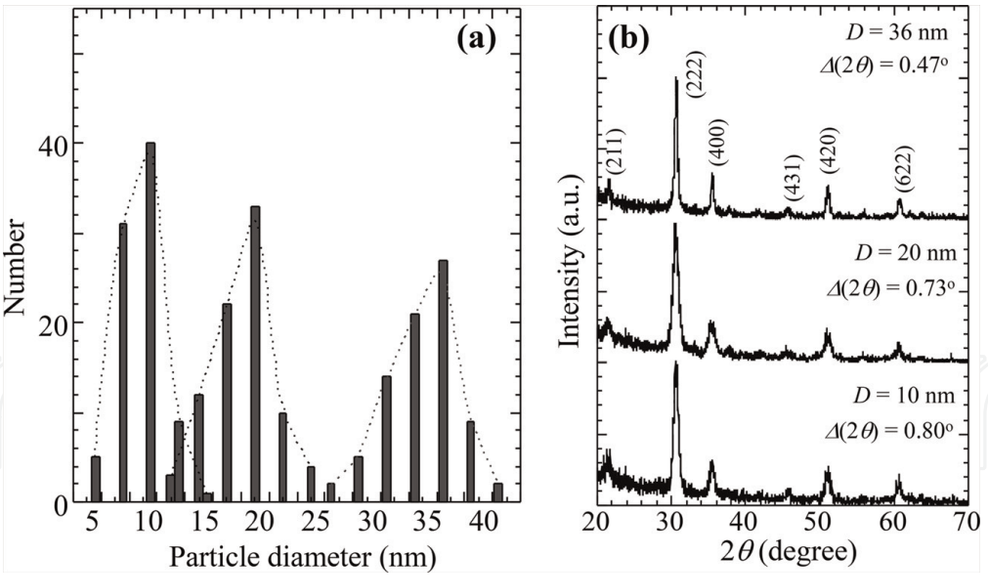

Figure 5.
(a) Size distributions of ITO NPs with particle sizes (D) of 10, 20, and 36 nm. Inset images show TEM images of ITO NPs with different particle sizes. (b) XRD 2q-q pattern of ITO NPs with D = 10, 20, and 36 nm. Δ(2θ) indicates a line-width of the (222) peak [25].

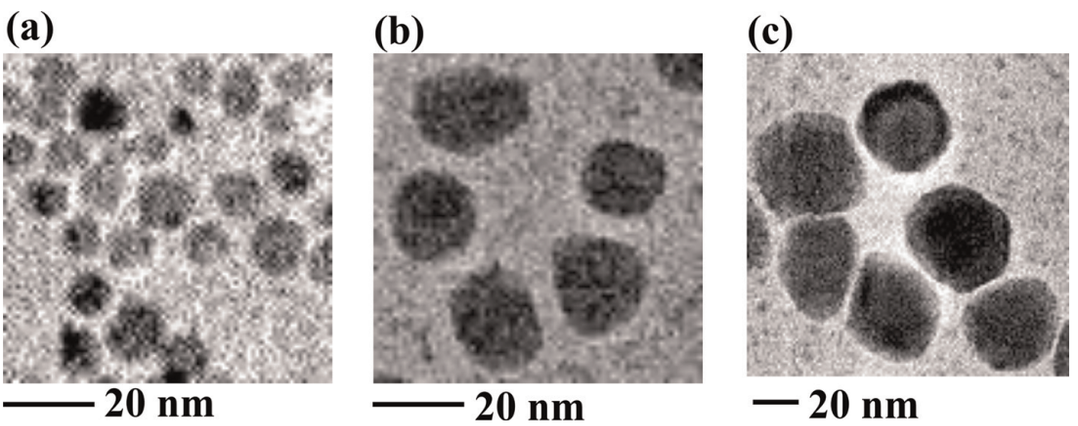

Figure 6.
TEM images of ITO NPs with D = 10 nm (a), 20 nm (b), and 36 nm (c) [25].

values of n_e were approximately 10^{21} cm^{-3}, and μ_e ranged from 21 to 37 $cm^2/V.s$. The broadening of the absorption spectra was related to the quality factor (*Q*-factor) of the plasmonic resonance defined by the ratio of peak energy to spectral linewidth of the LSPR peak. This factor provided a good indication of weak electronic damping and efficient *E*-field generation. *Q*-factor values of LSPRs with *D* = 10, 20, and 36 nm NPs were 2.4, 3.3, and 4.5 respectively. The increase in particle size is expected for strong *E*-field enhancement on the NP surfaces. It was indicated that the *Q*-factor values in the LSPR peaks were attributed to the electronic and crystalline properties. On the other hand, the LSPR peak positions were independent of particle size.

The peak positions of LPRs generally depend on the particle size in the case of metal NPs. The size-dependent absorption spectra of spherical NPs can be calculated precisely using the full Mie equations. These equations can describe well the size effects of LSPRs in metal NPs as follows.

An analytical solution to Maxwell's equations describes the extinction and scattering of light by spherical particles. The electromagnetic field produced by a plane wave incident on a homogeneous conducting sphere can be expressed by the following relations [26]:

$$\sigma_{ext} = \frac{2\rho}{|k|^2}\sum_{L=1}^{\infty}(2L+1)[\mathrm{Re}(a_L + b_L)] \tag{4}$$

where k is the incoming wave vector and L are integers representing the dipole, quadrupole, and higher multipoles of the scattering. In the above equations, a_L and b_L are represented by the following parameters, composed of the Riccati-Bessel functions ψ_L and χ_L [26]:

$$b_L = \frac{\psi_L(mx)\psi_L'(x) - m\psi_L'(mx)\psi_L(x)}{\psi_L(mx)\chi_L'(x) - m\psi_L'(mx)\chi_L(x)} \tag{5}$$

$$a_L = \frac{m\psi_L(mx)\psi_L'(x) - \psi_L'(mx)\psi_L(x)}{m\psi_L(mx)\chi_L'(x) - \psi_L'(mx)\chi_L(x)} \tag{6}$$

Here, $m = \tilde{n}/n_m$, where $\tilde{n} = n_R + in_I$ is the complex refractive index of the metal and n_m is the refractive index of the surrounding medium. Additionally, $x = k_m r$, where r is the radius of the particle. It should be noted that $k_m = 2\pi/\lambda_m$ is defined as the wavenumber in the medium rather than the vacuum wavenumber. Peak positions of absorption spectra of ITO NPs were estimated using the full Mie theory (black line in **Figure 7(b)**). The dielectric constants were taken from the ellipsometric data of an ITO film with an electron density of 1.0×10^{21} cm^{-3}. The estimated peak positions remained almost unchanged with particle sizes below 120 nm and then slightly redshifted to longer wavelengths with particle sizes above 120 nm. That is, ITO NPs with particle sizes below 40 nm had no high-order plasmon mode and were mainly dominated by light absorptions. These results differed largely from those of metal NPs. LSPR properties of ITO NPs could be fully described using Mie theory in the quasi-static limit.

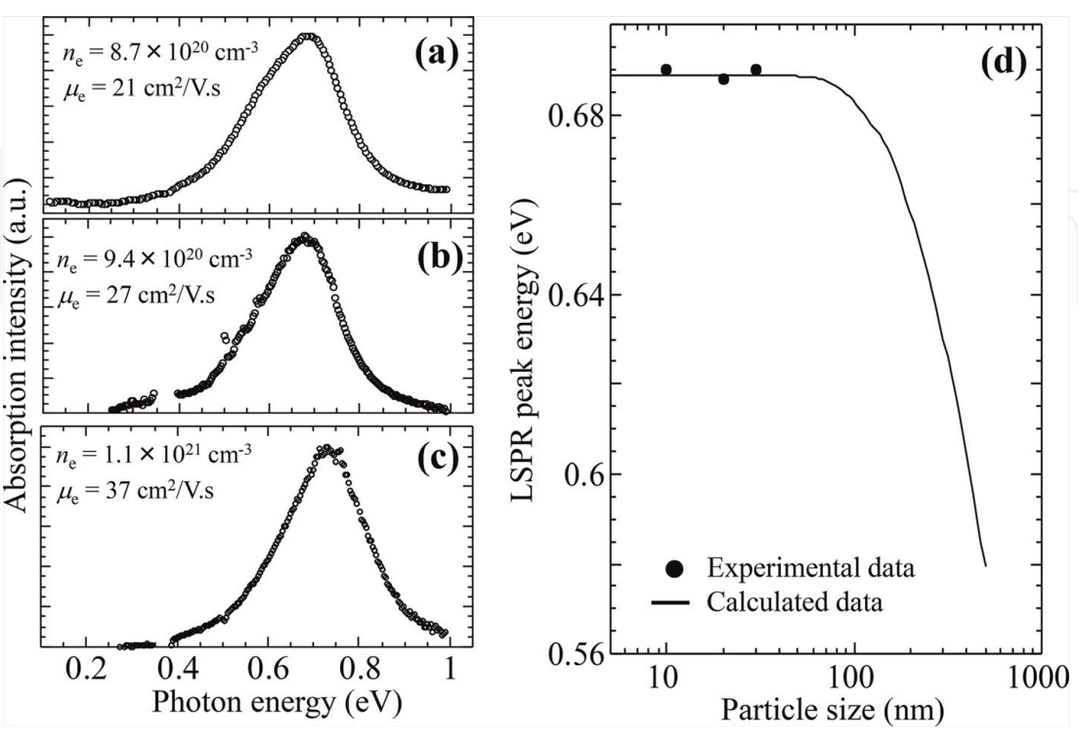

Figure 7.
(a) Absorption spectra of ITO NPs with different sizes comprising (a) 10 nm, (b) 20 nm, and (c) 36 nm. (d) LSPR peak energy as a function of particle size. A black line represents using Eqs. (4)–(6) [25].

4. Infrared applications for solar-thermal shielding

4.1 High reflections in the IR range

Recently, plasmonic properties on oxide semiconductors have attracted much attention in the area of solar-thermal shielding. The purpose of our study is to apply the plasmonic properties of assembled films of ITO NPs. To date, IR optical responses have been investigated with regard to transmittance and extinction spectra of composites and films using oxide semiconductor NPs. IR shielding properties by transmittance and absorption properties have mainly been discussed [27–30]. Reports concerning reflective performances in assemblies of NPs have yet to appear in spite of the desire for thermal shielding to cut IR radiation, not by absorption, but through reflection properties.

Assemblies of Ag and Au NPs can produce high *E*-fields through plasmon coupling between NPs in the visible range and are utilized in surface-enhanced spectroscopy [31, 32]. The high *E*-fields localized between NPs are very sensitive to interparticle gaps [33]. A gap length down to distances less than the size of a NP causes remarkable enhancements in *E*-fields. Surfactant- and additive-treated NPs are effective strategies that can be employed to obtain small interparticle gaps between NPs, which can be developed into one-, two-, and three-dimensional assemblies of NPs [34]. In particular, optical applications based on NPs have the benefit of large-area fabrications with lower costs to make NP assemblies attractive for industrial development.

In this section, we report on the plasmonic properties of assembled films comprising ITO NPs (ITO NP films) and their solar-thermal applications in the IR range [35]. Both experimental and theoretical approaches were employed in an effort to understand the plasmonic properties of the NP films. The IR reflectance of the NP films was analyzed on the basis of variations in particle size and electron density. The investigation focused in particular on *E*-field interactions in order to determine how the NP films affected high IR reflectance. This behavior is discussed in terms of the physical concept of plasmonic hybridization, which further clarified the importance of interparticle gaps for high IR reflectance.

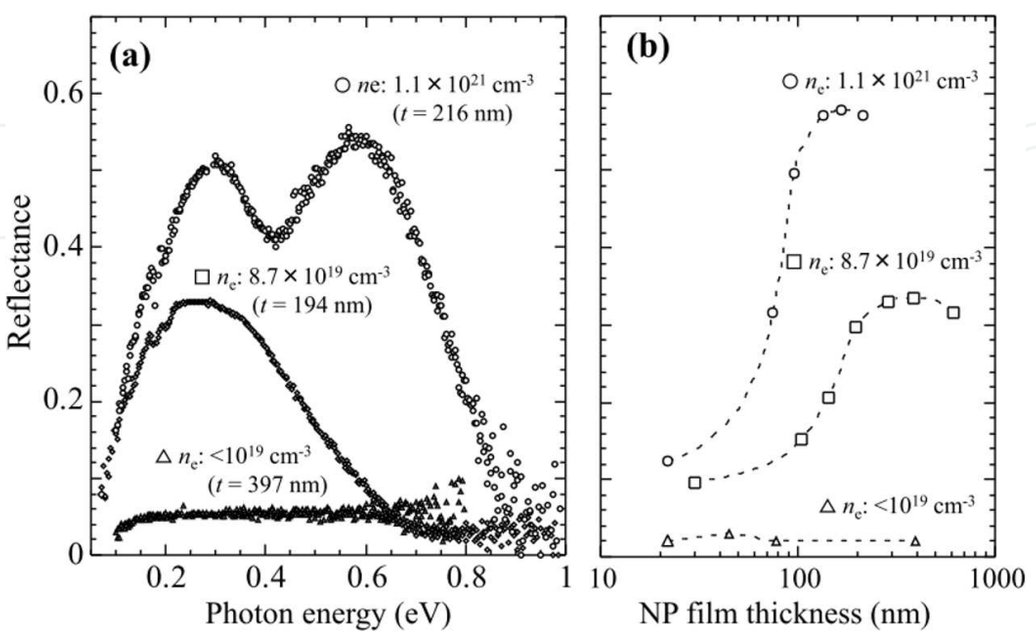

Figure 8.
(a) Reflectance spectra of ITO NP films with different electron densities of 1.1 × 10^{21} cm^{-3} (○), 8.7 × 10^{19} cm^{-3} (□), and < 10^{19} cm^{-3} (Δ). (b) Reflectance as a function of NP film thickness of ITO NP films with different electron densities.

Figure 8(a) shows reflectance spectra of ITO NP films with different electron densities. The assembled ITO NP films were deposited on IR-transparent CaF_2 substrates through a spin-coating technique. The spin-coating conditions comprised sequential centrifugation at (i) 800 rpm for 5 s, (ii) 2400 rpm for 30 s, and (iii) 800 rpm for 10 s. The fabricated NP films were then thermally treated at 150°C in air to evaporate the solvent. Reflectance was enhanced with increasing electron density and reached a value of ca. 0.6 in the NP film with $n_e = 1.1 \times 10^{21}$ cm^{-3}. Additionally, reflectance was dependent on film thickness (**Figure 8(b)**). Reflectance gradually increased with increasing film thickness and was then saturated in film thicknesses above 200 nm. As a result, it is necessary to use NPs with high electron density in order to obtain NP films with high IR reflectance.

Figure 9(a) shows reflectance spectra of ITO NP films with different particle sizes. Reflectance gradually increased with increasing particle size, which was dependent on NP film thickness (**Figure 9(b)**). That is, increasing in particle size contributed to obtain high IR reflectance. Highly efficient solar-thermal shielding played an important role in controlling electron density and particle size. We found that the high IR reflectance was closely related to plasmon coupling between the NPs in the NP films as follows.

4.2 Electric field distributions

Figure 10(a) shows experimental and theoretical absorption spectra of ITO NPs dispersed in toluene. The theoretical data was simulated using the finite-difference time-domain (FDTD) method and was close to the experimental data. We observed the formation of a strong electric field (E-field) on the NP surface (inset of **Figure 10(a)**). The relationship between the *E*-field and photon energy was further investigated, as shown in **Figure 10(b–d)**. The *E*-field on the NP surface increased with increasing photon energy. A high E-field was obtained at an LSPR peak position of 1.8 μm. The LSPRs of ITO NPs produced the strong E-field on the NP surface.

We evaluated the optical properties of ITO NP films from the viewpoint of electrodynamic simulations based on the finite-difference time-domain (FDTD) method (**Figure 11(a)**). The modeled NP layer was assumed to have a hexagonally close-packed (HCP) structure with an interparticle distance (*r*) of 2 nm along the in-plane

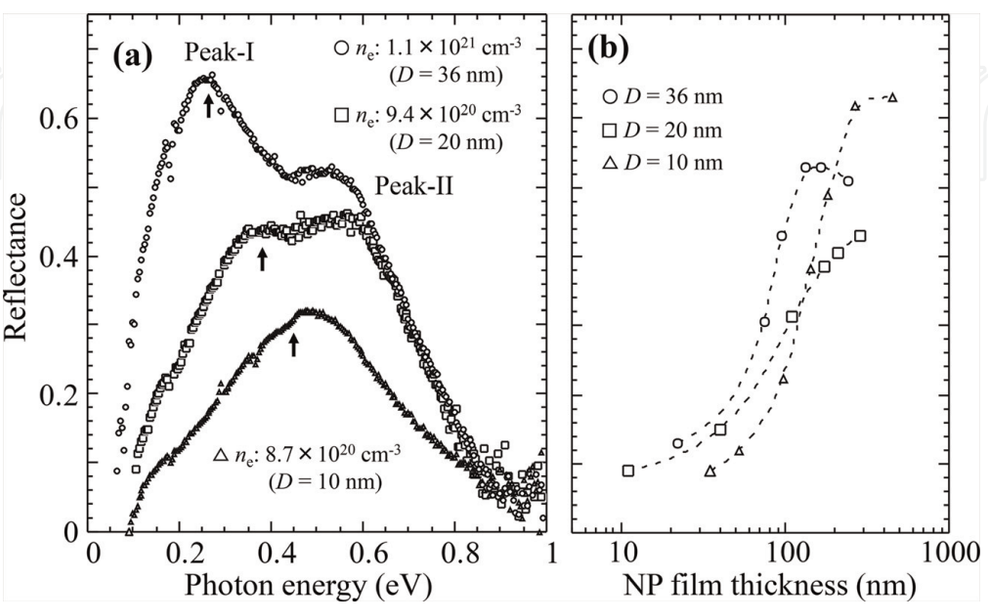

Figure 9.
(a) Reflectance spectra of ITO NP films with different particle sizes of 36 nm (○), 20 nm (□), and 10 nm (△). (b) Reflectance as a function of NP film thickness of ITO NP films with different particle sizes.

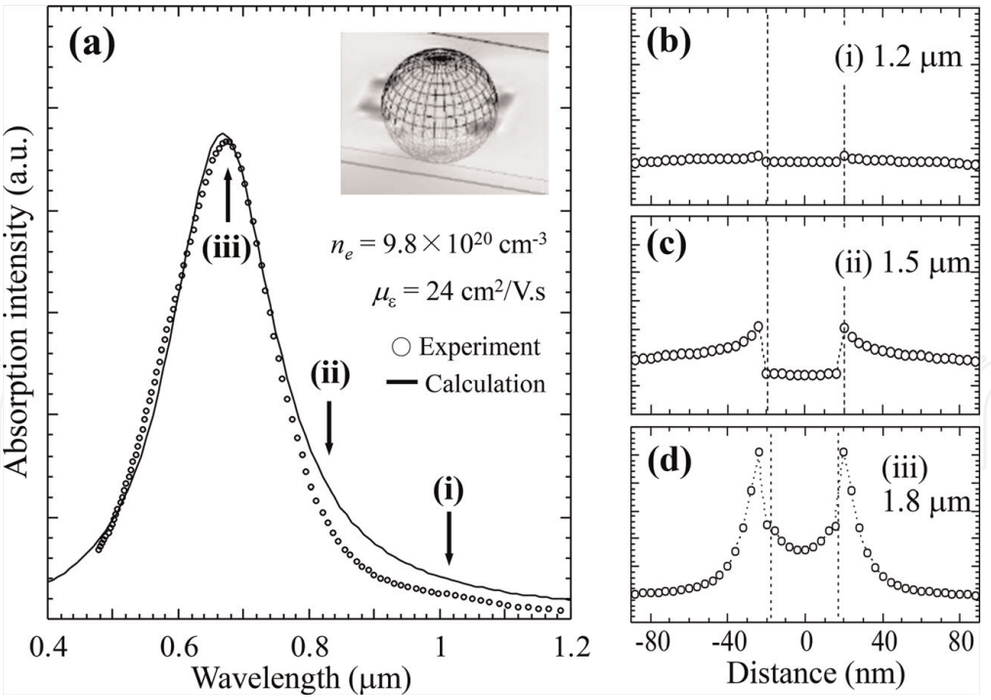

Figure 10.
(a) Absorption spectra of ITO NPs: Experimental (open circles) and simulated data (solid line). Inset indicates an electric field distribution on the NP surface obtained by the FDTD simulation. Cross-section field distributions at 1.2 μm (b), 1.5 μm (c), and 1.8 μm of the NPs.

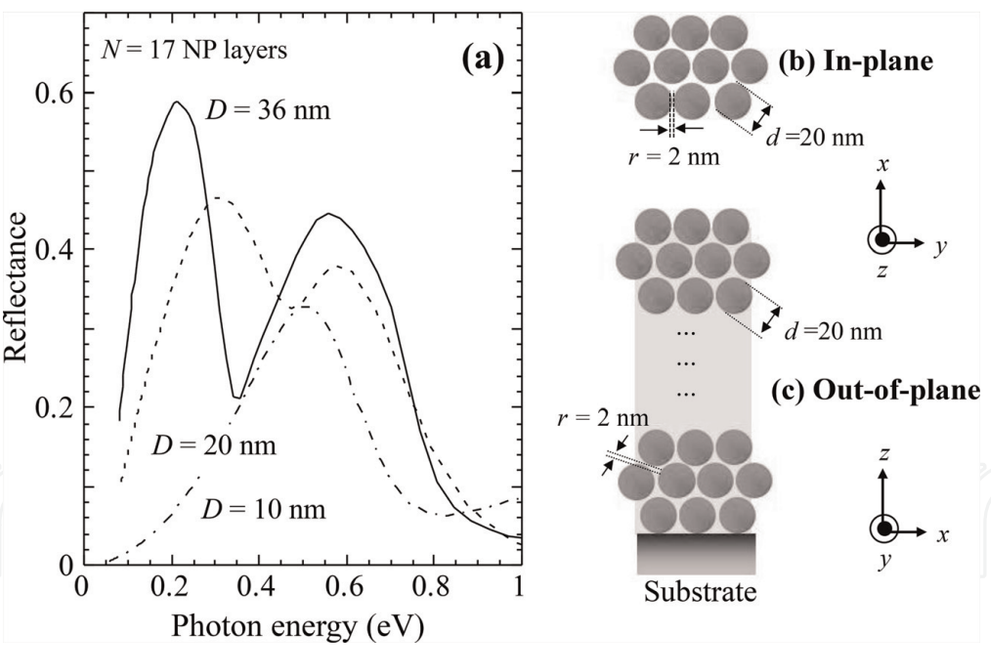

Figure 11.
(a) Simulated reflectance spectra of ITO NP layers at different particle sizes (D). A number of NP layer (N) was set to N = 20 NP layers. (b) and (c) indicate structural diagrams of a simulated NP layers along the in-plane (x-y) and out-of-plane (x-z) directions, respectively. The modeled structure was assumed to have a HCP structure with an interparticle distance (r) of 2 nm and was illuminated with light directed in the z direction from the air side. The E-field was parallel to the x direction.

(*x*-*y*) and out-of-plane (*y*-*z*) directions (**Figure 11(b** and **c)**). The modeled sample was illuminated with light directed in the *z* direction from the air side. The E-field was parallel to the x direction. The refractive index (real part: 1.437) of capric acid was used for the medium between the NPs. The dielectric functions of the ITO NPs were obtained from the parameter fitting for the absorption spectra. **Figure 11(a)** shows the reflectance spectra of ITO NP layers with different particle sizes (*D*) of 10, 20, and

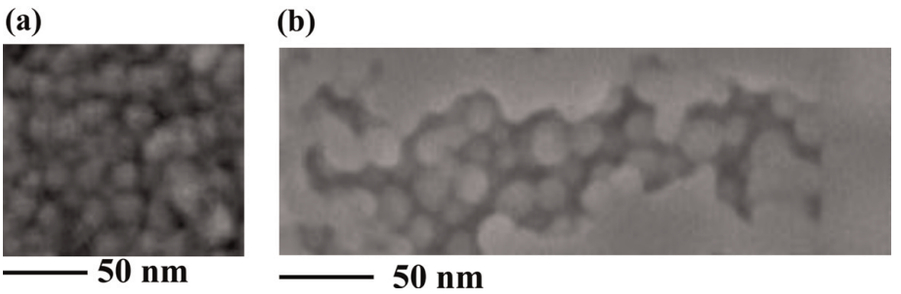

Figure 12.
SEM images of an ITO NP film along the in-plane (a) and out-of-plane (b) directions.

36 nm. The number of the NP layer was set to the N = 20 NP layer. Reflectance clearly enhanced with increasing particle size, which appeared as a result of three-dimensional assemblies of ITO NPs, and it was suggested theoretically that increasing particle size contributed to the reflective-type thermal shielding in the IR range.

Plasmon coupling between NPs produces large enhancements of E-fields at interparticle gaps. We typically investigated the E-field distributions at peak-II (0.60 eV) and peak-I (0.208 eV) for a 20 NP layer with D = 36 nm. **Figure 12(a** and **b)** shows SEM images of ITO NP films (D = 36 nm) along the in-plane and out-of-plane directions, revealing that the NPs had close-packed structures along both

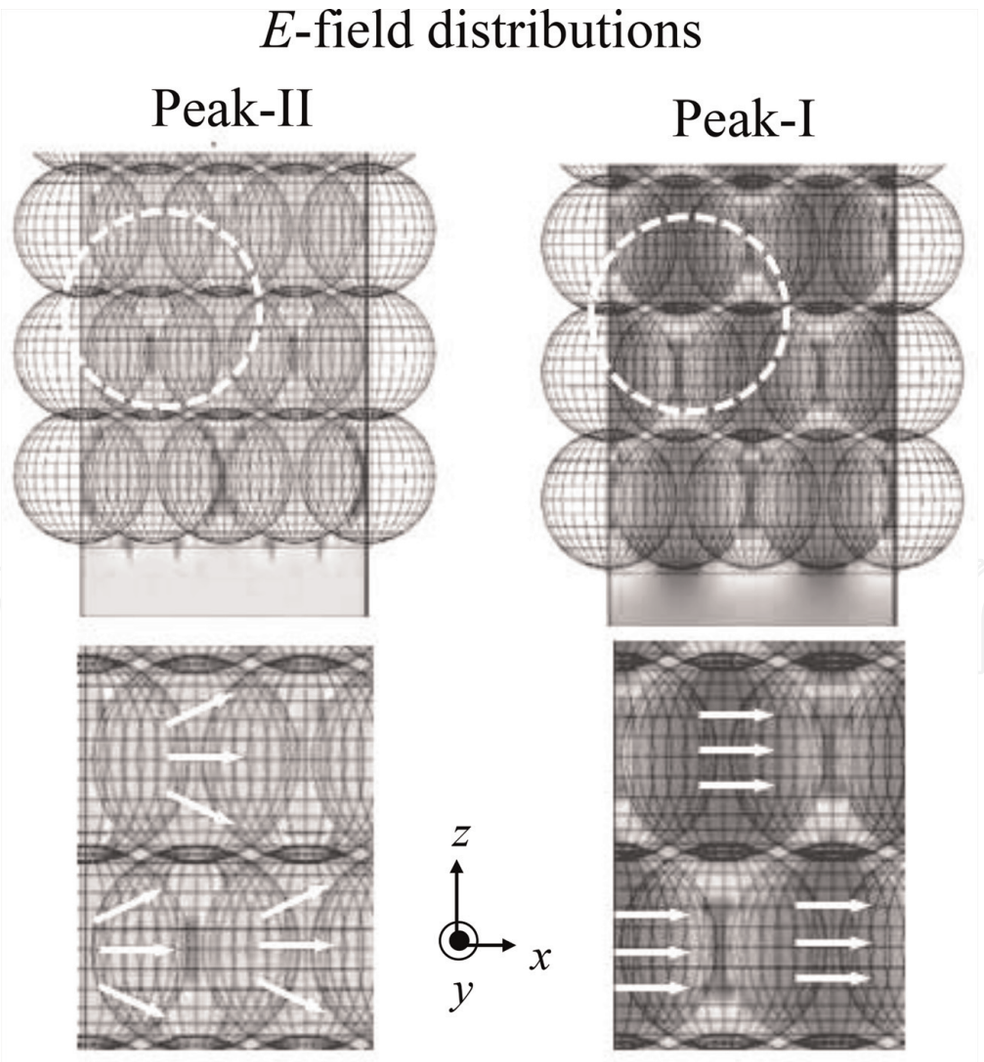

Figure 13.
Images of the E-field distributions and charge vectors at peak-I and peak-II along the x-z directions. Regions delimited by white circles were positioned in the respective bottom parts. An E-field was applied along the x direction. Light was incident along the z direction from the air side.

directions. **Figure 13** shows the *E*-field distributions along the *x*-*z* directions. For peak-I, the E-field between the NPs was strongly localized along the *x* direction when an electric field of light was applied along this direction. In contrast, peak-II displays *E*-fields along the diagonal directions in the *x*-*z* plane in addition to those along the *x* direction. A difference in the *E*-field of peak-I and peak-II was clearly found. The FDTD simulations revealed that the two types of reflectance peaks had different mechanisms of plasmon excitations. Therefore, it was indicated that different *E*-field distributions between the NPs played an important role in producing the IR reflectance in the IR range.

5. Conclusion

Optical properties of carrier- and size-dependent LSPRs were investigated using dopant-controlled ITO NPs. From systematic correlations between LSPR excitations and electron density, plasmon damping of ITO NPs was closely related to electron-impurity scattering, which was effective with high n_e values greater than 10^{20} cm^{-3}. That is, the role of electron carriers in ITO NPs could enhance LSPRs with simultaneous damped plasmon excitations. Changes in particle size also affected the LSPRs in ITO NPs. Increasing particle size altered the magnitude and peak splitting of the resonant reflectance, which covered a wide IR range. As a result, the carrier and size control of ITO NPs led to high solar-thermal shielding. The origin of the high IR reflectance of ITO NP films was clarified by electrodynamic simulations (FDTD). We found that the *E*-field distributions between the NPs along the in-plane and out-of-plane directions played key roles in producing the high IR reflectance. Control of electron carrier and particle size revealed important aspects that should be considered in the area of structural design when fabricating thermal-shielding materials.

Acknowledgements

This research was supported in part by a grant from JST A-Step (No. VP30218088667) and for Grant-in-Aids for Scientific Research (B) (No. 18H01468).

Conflict of interest

The authors declare no competing financial interest.

Author details

Hiroaki Matsui
Department of Bioengineering, Department of Electrical Engineering and Information Systems, The University of Tokyo, Tokyo, Japan

*Address all correspondence to: hiroaki@ee.t.u-tokyo.ac.jp

References

[1] Dastmalchi B, Tassin P, Koschny T, Soukoulis M. A new perspective on plasmonics: Confinement and propagation length of surface plasmons for different materials and geometries. Advanced Optical Materials. 2015;**4**(1):1-8. DOI: 10.1002/adom.201500446

[2] Khamh H, Sachet E, Kelly K, Maria JP, Franzen S. As good as gold and better: Conducting metal oxide materials for mid-infrared plasmonic applications. Journal of Materials Chemistry C. 2018;**6**:8326-8342. DOI: 10.1039/c7tc05760a

[3] Pgeifer P, Adinger U, Schwotzer G, Diekmann S, Steinrücke P. Real time sensing of specific molecular binding using surface plasmon resonance spectroscopy. Sensors and Actuators B. 1999;**54**:166-175. DOI: 10.1016/S0925-4005(98)00334-7

[4] Matsui H, Badalawa W, Ikehata A, Tabata H. Oxide surface plasmon resonance for a new sensing platform in the near-infrared range. Advanced Optical Materials. 2013;**1**:397-403. DOI: 10.1002/adom.201200075

[5] Matsui H, Ikehata A, Tabata H. Surface plasmon sensors on ZnO: Ga layer surfaces: Electric field distributions and absorption-sensitive enhancements. Applied Physics Letters. 2015;**106**:019905. DOI: 10.1063/1.4905211

[6] Matsui H, Ikehata A, Tabata H. Asymmetric plasmon structures on ZnO: Ga for high sensitivity in the infrared range. Applied Physics Letters. 2016;**109**:191601. DOI: 10.1063/1.4966598

[7] Lounis SD, Runnerstrom EL, Llordés A, Milliron DJ. Defect chemistry and plasmon physics of colloidal metal oxide nanocrystals. Journal of Physical Chemistry Letters. 2014;**5**:1564-1574. DOI: 10.1021/jz500440e

[8] Li SQ, Guo P, Buchholz DB, Zhou W, Hua Y, Odom TW, et al. Plasmonic-photonic mode coupling in indium-tin-oxide nanorods arrays. ACS Photonics. 2014;**1**:163-172. DOI: 10.1021/ph400038g

[9] Agrawal A, Kriegel I, Milliron DJ. Shape-dependent field enhancement and plasmon resonance of oxide nanocrystals. Journal of Physical Chemistry C. 2015;**119**:6227-6238. DOI: 10.1021/acs.jpcc.5b01648

[10] Furube A, Yoshinaga T, Kanehara M, Eguchi M, Teranishi T. Electric field enhancement inducing near-infrared two photon absorption in an indium tin oxide nanoparticle film. Angewandte Chemie. 2012;**51**:2640-2642. DOI: 10.1002/anie.201107450

[11] Matsui H, Badalawa W, Hasebe T, Furuta S, Nomura W, Yatsui T, et al. Coupling of Er light emissions to plasmon modes on In_2O_3: Sn nanoparticle sheets in the near-infrared range. Applied Physics Letters. 2104; **105**:041903. DOI: 10.1063/1.4892004

[12] Sönnichsen C, Franzl T, Wilk T, Plessen GV, Feldmann J. Drastic reduction of plasmon damping in gold nanorods. Physical Review Letters. 2002;**88**:077402. DOI: 10.1103/PhysRevLett.88.077402

[13] Sönnichsen C, Franzl T, Plessen GV, Feldmann J. Plasmon resonances in large noble-metal clusters. New Journal of Physics. 2002;**4**:93.1-93.8. DOI: 10.1088/1367-2630/4/1/393

[14] Berciand S, Cognet L, Tamarat P, Lounis B. Observation of intrinsic size effects in the optical response of individual gold nanoparticles. Nano Letters. 2005;**5**:515-518. DOI: 10.1021/nl050062t

[15] Langhammer C, Schwind M, Kasemo B, Zorić. Localized surface plasmon resonances in aluminum nanodisks. Nano Letters. 2008;**8**: 1461-1471. DOI: 10.1021/nl080453i

[16] Runnerstrom EL, Bergerud A, Agrawal A, Johns RW, Dahlman CJ, Singh A, et al. Defect engineering in plasmonic metal oxide nanocrystals. Nano Letters. 2016;**16**:3390-3398. DOI: 10.1021/acs.nanolett6b01171

[17] Rowe DJ, Jeong JS, Mkhoyan KA, Kortshagen UR. Phosphorus-doped silicon nanocrystals exhibiting mid-infrared localized surface plasmon resonance. Nano Letters. 2013;**13**: 1317-1332. DOI: 10.1021/nl4001184

[18] Schimpf AM, Lounis SD, Runnerstrom EL, Milliron DJ, Gamelin DR. Redox chemistries and plasmon energies of Photodoped In_2O_3 and Sn-doped In_2O_3 (ITO) nanocrystals. Journal of the American Chemical Society. 2015; **137**:518-524. DOI: 10.1021/ja5116953

[19] Matsui H, Furuta S, Tabata H. Role of electron carriers on local surface plasmon resonances in doped oxide semiconductor nanocrystals. Applied Physics Letters. 2014;**104**:211903. DOI: 10.1063/1.4880356

[20] Hartland GV. Optical studies of dynamics in noble metal nanostructures. Chemical Reviews. 2011;**111**:3857-3887. DOI: 10.1021/cr1002547

[21] Pisarkiewicz Y, Zakrzewska K, Leja E. Scattering of charge carriers in transport and conducting thin oxide films with a non-parabolic conduction band. Thin Solid Films. 1989;**174**: 217-223. DOI: 10.1016/0040-6090(89) 90892-4

[22] Pammi SV, Chanda A, Ahn JK, Park JH, Cho CR, Lee CR, et al. Low resistivity ITO thin films deposited by NCD technique at low temperature: Variation of tin concentration. Journal of the Electrochemistry of Society. 2010;**157**:H937-H941. DOI: 10.1149/ 1.3467802

[23] Mohammed HA. Effect of substrate temperature on physical properties of In_2O_3: Sn films deposited by e-beam technique. International Journal of Physical Sciences. 2012;**7**:20120-22109. DOI: 10.5897.IJPS12.182.

[24] Ku HY, Ullman FG. Capacitance of thin dielectric structures. Journal of Applied Physics. 1964;**35**:265. DOI: 10.1063/1.1713297

[25] Matsui H, Hasebe T, Hasuike N, Tabata H. Plasmonic heat shielding in the infrared range using oxide semiconductor nanoparticles based on Sn-doped In_2O_3: Effect of size and interparticle gap. ACS Applied Nano Materials. 2018;**1**:1853-1862. DOI: 10.1021/acsanm8b00260

[26] Mie G. Beiträge zur optik trüber medien, speziell kolloidaler metallösungen. Ann. Phys. 1908;**330**: 377. DOI: 10.1002/amdp19083300302

[27] Li SY, Niklasson GA, Granqvist CG. Plasmon-induced near-infrared electrochromism based on transparent conducting nanoparticles: Approximate performance limits. Applied Physics Letters. 2012;**101**:071903. DOI: 10.1063/ 1.4739792

[28] Katagiri K, Takabatake R, Inumaru K. Robust infrared-shielding coating films prepared using perhydropolysilazane and hydrophobized indium tin oxide nanoparticles with tuned surface plasmon resonances. ACS Applied Materials & Interfaces. 2013;**5**:10240-10245. DOI: 10.1021/am403011t

[29] Fang X, Mak CL, Dai J, Li K, Ye H, Leung CW. ITO/Au/ITO sandwich structure for near-infrared plasmonics. ACS Applied Materials & Interfaces. 2014;**6**:15743-15752. DOI: 10.1021/ am50261565

[30] Tao P, Viswanath A, Schadler LS, Benicewicz BC, Siegel RW. Preparation and properties of indium tin oxide/epoxy nanocomposites with Polyglycidyl methacrylate grafted nanoparticles. ACS Applied Materials & Interfaces. 2011;**3**:3638-3645. DOI: 10.1021/am200841n

[31] Tao AR, Ceperley DP, Sinsermsuksakul P, Neureuther AR, Yang P. Self-organized silver nanoparticles for three-dimensional plasmonic crystals. Nano Letters. 2008; **8**:4033-4038. DOI: 10.1021/nl802877h

[32] Chen CF, Tzeng SD, Chen HY, Lin KJ, Gwo S. Tunable plasmonic response from alkanethiolate-stabilized gold nanoparticle superlattices: Evidence of near-field coupling. Journal of the American Chemical Society. 2008;**130**: 824-826. DOI: 10.1021/ja0773610

[33] Le F, Brandl DW, Urzhumov YA, Wang H, Lundu J, Halas NJ, et al. Metallic nanoparticle arrays: A common substrate for both surface-enhanced Raman scattering and surface-enhanced infrared absorption. ACS Nano. 2008;**2**: 707-718. DOI: 10.1021/nn800047e

[34] Toma M, Toma K, Michioka K, Ikezoe Y, Obara D, Okamoto K, et al. Collective plasmon modes excited on a silver nanoparticle 2D crystalline sheet. Physical Chemistry Chemical Physics. 2011;**13**:7459-7466. DOI: 10.1039/cocp02953j

[35] Matsui H, Furuta S, Hasebe T, Tabata H. Plasmonic-field interactions at nanoparticle interfaces for infrared thermal-shielding applications based on transparent oxide semiconductors. ACS Applied Materials & Interfaces. 2016;**8**: 11749-11757. DOI: 10.1021/acsami6b01202